This is a preprint, the final version is subject to change, of the American Mineralogist (MSA)
Cite as Authors (Year) Title. American Mineralogist, in press.
(DOI will not work until issue is live.) DOI: http://dx.doi.org/10.2138/am-2015-5198

REVISION 1

Structural insights and elasticity of single-crystal antigorite from high-pressure Raman and Brillouin spectroscopy measured in the (010) plane

Hauke Marquardt[1*#], Sergio Speziale[1], Monika Koch-Müller[1], Katharina Marquardt[1*], Giancarlo Capitani[2]

1German Research Centre for Geosciences GFZ, Telegrafenberg, 14473 Potsdam, Germany,

2Dipartmento di Scienze dell'Ambiente, del Territorio e di Scienze della Tarra, Università di Milano Bicocca, P.za della Scienza 4, 20126 Milano, Italy

**present address: Bayerisches Geoinstitut BGI, University of Bayreuth, 95440 Bayreuth, Germany*

#Correspondence to: Hauke.Marquardt@uni-bayreuth.de, +49 921 553718

Abstract

We report high-pressure Raman and Brillouin spectroscopy results measured in the (010) plane of a natural antigorite single-crystal. We find that structural changes at >6 GPa lead to (1) an intensity crossover between Raman modes of the Si-O-Si bending vibrations, (2) changes of the compression behaviour of Raman modes related to the SiO_4 tetrahedra, (3) changes of the pressure derivative of the Raman shifts associated with OH stretching vibrations, (4) the emergence of a new Raman band in the OH spectral region, (5) a softening of the elastic constants c_{33} and c_{11}, and (6) a directional change of the slowest compressional wave velocity in a-c-plane. In addition to the structural insights at high-pressure, the unique characteristics of our

single-crystal sample allows for first direct measurements of the acoustic velocity anisotropy in a plane perpendicular to the basal **a**-**b**-plane. Comparison to previously published data indicates that the elastic anisotropy of antigorite strongly depends on the FeO and/or Al_2O_3 content. In contrast, it seems not to be affected by increasing temperature as inferred from an additional high temperature experiment performed in our study. These constraints are important for the interpretation of seismic anisotropy observations in subduction zone environments.

Keywords: Antigorite, Serpentine, elasticity, Brillouin, Raman, Seismic anisotropy

Introduction

Serpentine group minerals are characterized by a layered structure, where sheets of SiO_4 tetrahedra alternate along the **c** direction with sheets of $MgO_2(OH)_4$ octahedra. In antigorite, the high-pressure high-temperature (H*P*/H*T*) monoclinic form of serpentine, the layers show a pronounced curvature along the basal plane, which is accompanied by changes in the polarity of the tetrahedral layer (Capitani and Mellini, 2004; Capitani and Mellini, 2006). Antigorite is a major mineral phase in subduction environments and serves as important carrier of water from Earth's surface to the upper mantle (e.g. Ulmer and Trommsdorff, 1995; Wunder and Schreyer, 1997). Its breakdown reaction has been associated with local melting of the mantle wedge and deep Earth seismicity (Ulmer and Trommsdorff, 1995; Dobson et al., 2002; Hilairet et al., 2007). Recently, the markedly anisotropic frictional strength of the antigorite (001) basal surface has been related to the dynamics of slab motion and seismic activity at convergent margins (Campione and Capitani, 2013). A detailed characterisation of the H*P*/H*T* physical properties and chemical behavior of antigorite is important to understand its potential role for geophysical and

geochemical processes in subduction zone settings. As a consequence of its layered structure, antigorite is expected to show a strong direction dependence for many physical and chemical properties, including elasticity (e.g. Bezacier et al., 2010). Knowledge of the anisotropic elastic properties of antigorite as a function of chemical composition at pressure and temperature conditions relevant to subduction environments is essential to understand its contribution to observed seismic anisotropy and map its abundance, distribution and breakdown reaction (e.g. Katayama et al., 2009; Long, 2013; Reynard, 2013).

In a high-pressure Raman study in a diamond-anvil cell (DAC) on synthetic antigorite, Reynard and Wunder (2006) observed changes in the pressure-derivative of OH-related Raman modes at a pressure of about 7 GPa. In a later single-crystal x-ray diffraction study this observation was assigned to a pressure-induced structural modification that occurs in antigorite at a pressure of about 6 GPa, evidenced by discontinuous changes of volume and β-angle (Nestola et al., 2010). The experimental findings were confirmed by computations that provided additional details on the associated structural re-arrangements in antigorite (Capitani and Stixrude, 2012). Computational studies also predicted that the pressure-induced structural re-arrangement affects the elastic properties of serpentine at HP (Mookherjee and Stixrude, 2009; Mookherjee and Capitani, 2011; Tsuchiya, 2013). The maximum effect was predicted for some of the elastic constants describing properties in the crystallographic **c** direction (c_{33} and c_{13}) (Tsuchiya, 2013). An effect of the structural change on elasticity was later confirmed by high-pressure Brillouin spectroscopy (Bezacier et al., 2013). However, because minerals of the serpentine group show a strongly layered crystal structure and therefore exhibit pronounced cleavage, sample platelets were restricted to the basal **a**-**b**-plane (the natural cleavage plane). Because of this experimental limitation, the previous Brillouin scattering study could only provide indirect constraints on the

68 elasticity along **c**. Here, we report single-crystal Brillouin scattering and Raman spectroscopy
69 results to above 10 GPa, measured in the **a**-**c**-plane of a natural antigorite.

70

71 ## Materials and Methods

72 ### Sample preparation and characterisation:

73 Serpentine (antigorite) crystals were taken from natural rocks of the central part of the Malenco
74 serpentinite body in northern Italy (details in Mellini et al., 1987; Capitani and Mellini, 2004).
75 The recalculated average composition of the sample material is
76 $(Mg_{2.638}Fe_{0.102}Al_{0.047}Cr_{0.014}Ni_{0.003}Mn_{0.002})_{\Sigma=2.808}(Si_{1.971}Al_{0.029})_{\Sigma=2}O_5(OH)_{3.647}$ (Capitani and Mellini,
77 2006). To facilitate single-crystal measurements in the (010) plane of antigorite, we employed the
78 focused ion beam preparation method (Marquardt and Marquardt, 2012). A FEI Quanta 3D at the
79 German Research Center for Geosciences (GFZ) Potsdam was operated at an accelerating voltage
80 of 30 keV and sample cutting was performed with 15 nA beam current. The current was
81 decreased to 7 nA for polishing. More details about the sample preparation can be found in
82 Marquardt and Marquardt (2012). We prepared a face-parallel platelet about 50×80 μm^2 wide and
83 30 μm thick (Fig. 1a). In addition, a ~100 nm thin lamella for characterisation by transmission
84 electron microscopy (TEM) was cut parallel to the platelet that was prepared for optical
85 spectroscopy (Fig. 1b). The TEM lamella extends to roughly half of the width of the DAC sample
86 platelet. The TEM analysis, which was carried out at the Bayerisches Geoinstitut BGI using a FEI
87 TITAN 80-200 at 200 keV, showed that the antigorite sample consists of several single-crystals
88 with a maximum misorientation smaller than 5°. For our analysis, we treat the sample as a single-
89 crystal. To acquire an electron diffraction pattern (Fig. 1c), the TEM-lamella (that was prepared
90 parallel to the sample platelet for optical spectroscopy) was tilted in the TEM by about 5° around

the [100]-direction and about 1° around the [001]-direction to align the [010] zone axis with the incoming electron beam. The effect of this slight misorientation on the derived acoustic velocities by Brillouin Spectroscopy is <0.1% and <1% at all experimental pressures for propagation of compressional velocities along the [100] and [001]-directions, respectively (based on the elastic constants reported by Mookherjee and Capitani, 2011).

Diamond-anvil cell setup:

The antigorite single-crystal was loaded in a symmetric diamond-anvil cell using diamonds with 600 μm-sized culets, a stainless-steel gasket pre-indented to 50 μm final thickness and a methanol-ethanol-water mixture (MEW) as pressure-transmitting medium. Pressure in the sample-chamber was determined by ruby fluorescence using the calibration of Mao et al. (1986). An additional high-temperature experiment was performed in a resistive-heated BX-90 diamond-anvil cell to a maximum temperature of 200°C (Kantor et al., 2012), but no pressure was applied. Temperature was determined by a Pt/PtRh-thermocouple attached to the side of one diamond-anvil.

Raman and Brillouin Spectroscopy:

High-pressure Raman spectroscopy was performed using a Horiba Jobin Yvon Labram HR 800 UV-VIS spectrometer (gratings 1800 lines/mm) in a backscattered configuration with a blue solid state laser (473 nm), a CCD detector and an Olympus optical microscope with a long working distance 20× objective. A confocal setup with a 100 μm slit was used. The spectrometer was calibrated at each pressure increase. Spectra were collected for 10 seconds with three accumulations from 100 to 1400 cm^{-1} and 2800 to 4000 cm^{-1}. At the highest pressure applied and upon decompression, spectra were collected from 3400 to 3850 cm^{-1} and the sample was rotated with respect to the inherent polarization of the excitation laser stepwise in 10° from 0° to 180°.

Raman spectra were collected at each angle for 30 seconds with six accumulations. After decompression the cell was opened and spectra were again collected in angular steps of 10°. Raman spectra were fit using Voigt peak shapes assuming a linear background.

High-pressure Brillouin scattering was carried out using the Brillouin spectroscopy system at the German Research Center for Geosciences with a scattering angle of 60°. The system uses a Nd:YVO_4 solid state laser operating at a wavelength of 532 nm as light source and a Sandercock-type tandem six-pass Fabry-Perot interferometer equipped with a photomultiplier tube for signal detection.

Results and discussion

Raman Spectroscopy

Lattice vibrations: Figure 2 shows representative Raman spectra collected at different pressures and in two different spectral regions along with the best-fit models. Fig. 2a shows a spectrum collected at 0.7 GPa in the low wavenumber region. The major vibration bands that were followed to high pressures are labelled and their pressure dependence is shown in Fig. 3. The spectrum is dominated by intense bands at 230 cm^{-1} (LV2), 374.6 cm^{-1} (LV3), 681.6 cm^{-1} (LV7), and 1044.7 cm^{-1} (LV11), where reported wavenumbers refer to the value at ambient pressure (Tab. 1). LV2 can be attributed to vibrations of the O-H-O groups (Rinaudo et al., 2003) and/or metal-oxygen vibrations (Auzende et al., 2004). LV3 is caused by symmetric vibrations of the SiO_4 tetrahedra (Rinaudo et al., 2003). LV7 and LV11 can be assigned to Si-O-Si bending modes (Rinaudo et al., 2003; Reynard and Wunder, 2006).

The frequencies of these major bands is in good agreement with previously reported Raman data for powdered synthetic pure Mg-antigorite (Reynard and Wunder, 2006) and natural antigorite (Rinaudo et al., 2003; Auzende et al., 2004) (except for LV11, which was outside of the spectral

range investigated by Auzende et al., 2004). In agreement with Reynard and Wunder (2006) (their Fig. 1), we see additional smaller vibration bands (or shoulders to main bands) at 198.5 cm^{-1} (LV1), 459 cm^{-1} (LV4), 528.8 cm^{-1} (LV5), and 636.1 cm^{-1} (LV6). In contrast to the study of Reynard and Wunder (2006), we can clearly resolve (and track to high-pressure) two additional Raman bands at 881.3 cm^{-1} (LV9) and 1028.8 cm^{-1} (LV10). Based on a theoretical study on lizardite, Raman bands at around 1000 cm^{-1} are likely related to Si-O stretching modes (Balan et al., 2002). The fact that these features were not observed in the previous study on pure synthetic antigorite suggests that they are related to the more complex chemistry of our natural sample. However, this may also be related to effects of crystallographic orientation on the Raman scattering intensity of these bands. Reynard and Wunder (2006) performed Raman spectroscopy measurement on a powder sample that likely shows a preferred orientation of the basal plane parallel to the diamond anvil culets caused by the strong cleavage, whereas we measured a single-crystal with the **a**-**c**-plane parallel to the diamond-culets.

The pressure-dependences of the main Raman bands are generally in good agreement with the previous studies (Tab. 1, Fig. 4a), with the exception of the lattice mode(s) at around 690 cm^{-1} (LV7 and LV8), which are associated with Si-O-Si bending vibrations (Reynard and Wunder, 2006). Both previous high-pressure studies assumed that this feature is dominated by a strong band (at 685-688 cm^{-1}) accompanied by a weak shoulder. However, our high-pressure single-crystal spectra clearly show that the intensity of LV7 substantially decreases with increasing pressure, whereas the intensity of LV8 (the "shoulder") simultaneously increases (Fig. 3). It is thus likely that the previous studies followed LV7 at low pressures, where it dominates the spectral feature, but switched to tracking LV8 at elevated pressures. This observation explains the very high pressure-derivative reported for that feature and it might also provide explanation for the large disagreement of the inferred pressure-derivatives between the two previous works,

which remained unexplained by Reynard and Wunder (2006). When applying a linear fit between v_{LV4} (0 GPa) and v_{LV5} (10 GPa), we obtain dv/dP = 5.7 cm^{-1}/GPa, which is in closer agreement with the pressure-derivative reported by Reynard and Wunder (2006). Even though the relative amplitudes of LV7 and LV8 change gradually with pressure the amplitude "crossover" takes place at around 6 GPa. This corresponds to the pressure, where an anomalous volume softening was previously observed experimentally (Nestola et al., 2010) and confirmed by recent computations (Capitani and Stixrude, 2012), indicating that the amplitude crossover might be triggered by a structural change. The computational study predicted a substantial change of the Si-O-Si bond angle in the tetrahedral layer with pressure as a result of a gradual change in the compression mechanism, which may be reflected in the intensity crossover of LV7 and LV8. This conclusion is supported by our observation that LV3 and LV11, which are both associated with vibrational modes related to the SiO_4 tetrahedra (Rinaudo et al., 2003), also show changes of pressure dependence at around 7 GPa (Fig. 4b).

OH stretching vibrations: In serpentine minerals, hydrogens are bond to the oxygen atoms that form the octahedral layer (O3, O4). Two different general positions exist for the hydrogen atoms. Either the hydrogen is pointing towards the center of the tetrahedral rings (H4, OH_{inner}), where it is in a similar environment as in talc (Stixrude, 2002) or it is located in between the octahedral and tetrahedral layers (H3, OH_{outer}). The OH_{inner}---O angle is 180° and the vector is oriented along **c**, whereas the OH_{outer}---O angle is 165.6° (measured at 8K in lizardite) and the O-H bond is not strictly oriented along **c** but points towards the nearest oxygen ion of the tetrahedral layer to form a hydrogen bond (Gregorkiewitz et al., 1996). Generally, the smaller bond length observed by neutron diffraction for the O-H_{inner} bond (0.8 Å) compared to the O-H_{outer} bond (1.16 Å),

suggests a weaker hydrogen bond of OH_{inner}---O than for OH_{outer}---O (Gregorkiewitz et al., 1996; Capitani and Stixrude, 2012; Noguchi et al., 2012).

In the spectral region characteristic for OH stretching-related modes, two strong vibration bands, accompanied by several shoulders (Fig. 2b), are clearly visible at low pressures. The position and pressure trends of the two main bands are in good agreement with the previous Raman spectroscopy studies (Tab. 1, Fig. 4c) and they can be assigned to the in-phase stretching mode of OH_{outer} (at 3669 cm^{-1}) and the stretching mode of OH_{inner} (at 3699 cm^{-1}) (Balan et al., 2002; Auzende et al., 2004; Reynard and Wunder, 2006). The bands at ~3700 cm^{-1} and ~3768 cm^{-1} may be caused by stretching vibrations of the inner OH, where the neighboring octahedral contain Fe-atoms substituting for Mg (e.g. Auzende et al., 2004)**.** The observed bands at ~3650 cm^{-1} and ~3610 cm^{-1} may correspond to out-of-phase stretching modes of the outer OH groups (Balan et al., 2002) with different occupancies of the surrounding octahedral positions (most likely 3 × Mg or 2 × Mg and 1 × Fe). Those modes show a slightly negative pressure trend (~1cm^{-1}/GPa), supporting the observations by Auzende et al. (2004).

Upon compression, the interlayer distance in serpentine minerals decreases and therefore an increase in hydrogen bonds of OH_{outer} could be expected, which would lead to a decrease of the Raman frequency of the covalent OH stretching vibration with pressure (Libowitzky, 1999). The experimentally observed positive pressure derivative of the Raman shift of the OH_{outer} stretching vibrations, however, indicates that the strength of hydrogen bonding does not increase. This observation can be explained by computational predictions for serpentine (lizardite and antigorite) indicating that the OH_{outer}---O angle progressively changes upon compression as a result of decreasing misfit between octahedral and tetrahedral layers caused by their different compression behaviour (Mookherjee and Stixrude, 2009; Capitani and Stixrude, 2012; Tsuchiya, 2013).

At pressures >6-7 GPa, both OH modes show an increased dependence on pressure (more pronounced for OH_{outer}). This change in dν/dP is likely associated with a proton reorientation as predicted from computations (Mookherjee and Stixrude, 2009; Capitani and Stixrude, 2012; Tsuchiya, 2013) and inferred from recent infrared spectroscopy measurements (Noguchi et al., 2012). A change of the pressure derivative of the OH_{outer} stretching mode is also visible in the data shown by Reynard and Wunder (2006), but was attributed to uncertainties in fitting caused by a strong overlap of Raman bands. The previous infrared study (Noguchi et al., 2012) reported a change of dν/dP for the OH_{outer} stretching vibration from 4.1 cm^{-1}/GPa below 5.3 GPa to 7.1 cm^{-1}/GPa at pressures >5.3 GPa, which is substantially different from our observations (1.6(2) and 6.3(4) cm^{-1}/GPa). This discrepancy may be related to the presence of non-hydrostatic stresses in the solid KBr pressure-transmitting medium used by Noguchi et al., 2012 (see Fig. 6 in Koch-Müller et al., 2011).

At pressures above 6-7 GPa, we observe the appearance of a third strong Raman band at 3730 cm^{-1} that shifts rapidly to larger wavenumbers when pressure is increased (Fig. 4c). The emergence of this band may be related to a symmetry-breaking response to compression above 6 GPa as inferred from computations (Capitani and Stixrude, 2012). Based on the pressure-evolution of our Raman spectra (Fig. 3), we cannot find any evidence that this vibration band was contributing to the spectrum at lower pressures as suggested by Reynard and Wunder (2006).

Figure 5 shows the change of Raman scattering intensity of the inner and outer OH mode with rotation of the DAC. The rotation angle was defined as zero when the **a** axis was optically aligned with the polarization direction of the incoming laser and as 90°, when the laser polarization was parallel to **c**. In the measurements that we performed out of the DAC, the scattering amplitude of the inner OH mode is strongest when the polarization of the laser is about parallel to **c**, i.e. parallel to the OH-vector. The outer OH mode, however, shows a maximum of

Raman scattering amplitude at about 70° (i.e. 20° from the **c** axis) and a secondary smaller maximum at about 110°. This observation supports the computational results that show a deviation of O-H_{outer} bond direction from the **c** direction in antigorite (Capitani and Stixrude, 2012) and is also in agreement with observations and computations on lizardite (Gregorkiewitz et al., 1996; Balan et al., 2002; Mookherjee and Stixrude, 2009). Upon pressure increase, the intensity maxima of both the inner and outer OH modes shift to ~110°, likely as a result of the optical properties of the strained diamond-anvils that affect the laser polarization. Interestingly, at high-pressures the intensity maximum as well as the dependence of intensity on rotation angle are almost identical for the inner and outer OH modes, indicating a similar orientation of the OH-vectors. Computational studies on antigorite and lizardite predicted that the angle the O-H_{outer} bond forms with the **c** direction decreases upon compression and ultimately vanishes (Mookherjee and Stixrude, 2009; Capitani and Stixrude, 2012) as a result of the difference in compression behaviour of the tetrahedral and octahedral layers. Our study provides direct support for the computational prediction and further indicates that this effect takes place already at pressures < 3 GPa in agreement with the considerations of Noguchi et al. (2012).

Brillouin Scattering

Figure 6a shows a representative Brillouin spectrum collected at high pressures. The compressional and one shear mode are clearly visible and well separated from the contribution of the pressure-transmitting medium (MEW). We observed signal for the acoustic shear wave velocities in many spectra. However, often only one shear mode was resolvable resulting in an incomplete angular coverage. Therefore, we focus our discussion on the compressional wave velocities that were of excellent quality at all rotation angles and exhibit a strong anisotropy

between the basal plane and the **c**-direction. Fig. 6b depicts the distribution of compressional velocities measured in the **a**-**c**-plane. At 0.7 GPa, we measured Brillouin scattering in an angular range from 0° to 180°. We found that our measurements can be well fit by assuming orthorhombic symmetry (in the following discussion, we will therefore neglect the small deviation of the β-angle from 90°). At all experimental pressures, the maximum compressional velocity is observed along **a**, i.e. parallel to the structural layers. The lowest observed compressional sound velocity is observed at around 60° (and 120°) from the **a** axis at low pressures. Upon pressure increase, the angle of minimum compressional velocity progressively shifts towards the basal plane. At 7.1 GPa (open symbols), the slowest compressional velocity is observed at an angle intermediate between **a** and **c**. Increasing pressure leads to a more pronounced velocity difference between the minimum velocity and the velocity along **c**. Fig. 6c illustrates the pressure dependence of the angular shift of the lowest observed compressional velocity. Our experimental data are in very good agreement with the computational predictions shown as grey circles (Mookherjee and Capitani, 2011).

Figure 7 summarizes the pressure-dependent compressional velocities measured along specific propagation directions. We observe a strong increase of compressional velocities along the **c** direction consistent with a progressive compression of the **c** axis and consequent elastic stiffening along this direction. The compressional velocity along **a** direction decreases with pressure, but is much less sensitive to a pressure increase.

At pressure >6 GPa, we observe a "softening" of the compressional velocity along **a** and a large decrease of the pressure dependence of the velocity along **c,** which is controlled by the elastic constant c_{33}. This observation is in agreement with previous predictions based on single-crystal x-ray diffraction (Nestola et al., 2010) and with computational studies on lizardite (Mookherjee and Stixrude, 2009; Tsuchiya, 2013). In contrast, a previous Brillouin scattering study reported a

small decrease of the pressure dependence of the compressional velocity along the **c** direction, but no effect on compressional velocities along **a** and **b** (Bezacier et al., 2013). According to computations, the elastic softening in antigorite is caused by a change of the dominant compression mechanism from a decrease of interlayer thickness to in-plane rotations of the SiO_4-tetrahedra (ditrigonalization) (Capitani and Stixrude, 2012). The same mechanism, which is also expected in lizardite (Mookherjee and Stixrude, 2009) and talc (Stixrude, 2002), causes the observed changes in the Raman spectra.

We compare our results with previous experimental studies (Bezacier et al., 2010; Bezacier et al., 2013) and computational predictions (Mookherjee and Capitani, 2011) in Fig. 7a. We note that there are some inconsistencies in the paper of Bezacier et al. (2013) (and Bezacier et al., 2010) regarding the assignment of the **a**- and **b**-directions to the elastic constants c_{11} and c_{22}. It is stated that c_{11} refers to the longitudinal constant along **a** and c_{22} refers to the constant along the **b**. Then, the minimum compressibility is reported along **b**, but c_{22} is smaller than c_{11}. For the following discussion, we assume that the largest elastic constant reported in the paper of Bezacier et al., 2013 corresponds to c_{22} and determines longitudinal wave propagation along **b**, making it the fastest direction consistent with computational data (Mookherjee and Capitani, 2011), the compressibility data from single-crystal x-ray diffraction (Nestola et al., 2010) and the results of our study.

After making this correction, there is qualitative agreement between our results and the studies by Mookherjee and Capitani (2011) and Bezacier et al. (2013) at pressures between 2 GPa and 6 GPa. However, our results do not agree at low pressures and at pressures > 6 GPa with the results of Bezacier et al. (2010) and Bezacier et al. (2013). This discrepancy may be caused by the experimental setup used in the studies by Bezacier and coauthors, where (a) Brillouin scattering was performed on a non-polished **a**-**b**-plane (natural cleavage plane) but parallelism of the

entering and exiting sample face is a strong requirement for optimal velocity determination in the DAC (Speziale et al., 2014), (b) sound wave velocities along the **c** direction were inferred from measurements in a backscattering geometry, which requires knowing the high-pressure refractive index of the sample at high pressure (Speziale et al., 2014).

However, there appears to be very good agreement between the derived pressure trends in the two experimental data sets at pressures between 2 GPa and 6 GPa. We, therefore, assume that the differences in absolute velocities are mostly related to compositional differences between our antigorite sample and the one studied by Bezacier et al. (2013). Their sample contains more iron (4.15 wt.% FeO) and aluminium (3.45 wt.% Al_2O_3) compared to our sample (2.65 wt.% FeO, 1.39 wt.% Al_2O_3) (Auzende et al., 2004; Capitani and Mellini, 2004). The different results from this study and the previous one then lead to different results of expected elastic anisotropy shown in Fig. 7b. Assuming that the observed discrepancies are caused by chemical variations, we infer that the addition of iron and/or aluminium to antigorite decreases the compressional wave anisotropy (defined as $(v_{p,a}-v_{p,c})/(v_{p,a}+v_{p,c})*200$, where the subscripts p, a and c refer to longitudinal polarization, **a** and **c** crystallographic directions respectively). This conclusion is consistent with the computational data on "ideal" $Mg_{48}Si_{34}O_{85}(OH)_{62}$ antigorite, showing stronger elastic anisotropy than found in both experimental studies on natural samples.

Additional room pressure measurements have been performed along a single crystallographic direction, close to the **b** axis (Fig. 7c) to place constraints on the effect of composition on shear wave polarization anisotropy. We selected a natural single-crystal platelet from our sample material and we used it unpolished as in the previous Brillouin scattering studies (Bezacier et al., 2010; Bezacier et al., 2013). We determined a polarization anisotropy along the **b** direction, which was optically identified from the sample's shape, of 68(2) % at room pressure, which is in between the anisotropies measured by Bezacier et al. (2010) (75 %) and the computational

predictions by Mookherjee and Capitani (2011) (53 %), indicating that a higher iron/aluminium content increases the shear wave polarization anisotropy (at least along **b**). We then resistively heated the DAC up to 200°C (at ambient pressure) to track the evolution of shear anisotropy with increasing temperature (Fig. 7c). Over the studied temperature range, the shear wave polarization anisotropy does not change within the uncertainties of the measurements. Also, the compressional wave velocity along **b** (determined by the elastic constant c_{22}) does not visibly change with increasing temperature.

Implications

We provide first direct measurements of compressional wave velocity anisotropy in the (010) plane of natural antigorite to high-pressure. By comparison to previously published data, we infer that the velocity anisotropy of antigorite is sensitive to variations in the Fe- and/or Al-content, whereas preliminary H*T*-results indicate that the elastic anisotropy is independent of temperature within the studied temperature range. Fig. 8 shows the potential behaviour of compressional sound wave anisotropy and shear polarization anisotropy with FeO (Figs. 8a, c) and Al_2O_3 (Figs. 8b, d) content. A recent compilation of the chemical composition of natural serpentine minerals found that the FeO content mostly falls between 6 and 10 wt.%, but can be as high as 12 wt.% for serpentinites from the mantle wedge (Deschamps et al., 2013). All antigorite compositions that have been studied for single-crystal elastic anisotropy have a lower iron content (Mookherjee and Capitani, 2011; Bezacier et al., 2013, this study). If the elastic anisotropy is indeed very sensitive to the iron content of antigorite, it is possible that antigorite in subduction environments is elastically less anisotropic for p-waves and more anisotropic for s-waves than previously assumed. Future studies should focus on the effect of chemical variations on anisotropy to allow

for mapping the hydration state in subduction environments through analysis of shear wave splitting or based on compressional azimuthal anisotropy data, which may become available in the future.

Acknowledgement: This work was supported by the DFG grants SP1216/3-1 and MA4534/3-1.

355 Table 1: Summary of Raman Spectroscopy results.

This study				Reynard & Wunder		Auzende et al. 2004	
mode	*P*-region of fit	ν (cm^{-1})	dν/d*P* (cm^{-1}/GPa)	ν (cm^{-1})	dν/d*P* (cm^{-1}/GPa)	ν (cm^{-1})	dν/d*P* (cm^{-1}/GPa)
LV1	0-6 GPa	198.5 (11)	1.9 (3)	-	-	-	-
LV2	0-10 GPa	230.0 (8)	5.0 (1)	229	4.7(3)	235	4.8 (2)
LV3	0-6 GPa	374.6 (5)	3.3 (1)	378	3.2 (1)	377	4.1 (1)
LV3	7-10 GPa	354.8(50)	5.9 (6)	-	-	-	-
LV4	0-4 GPa	459.1 (4)	3.9 (1)	459	4.6 (4)	-	-
LV5	0-8 GPa	528.8 (8)	3.0 (2)	-	-	-	-
LV6[#]	0-10 GPa	636.1 (24)	3.9 (4)	-	-	-	-
LV7*	0-6 GPa	681.6 (10)	2.8 (3)	688	6.5 (8)	685	4.9 (2)
LV8*	4-10 GPa	704.3 (16)	2.9 (2)	-	-	-	-
LV9	0-8 GPa	881.3 (9)	3.5 (2)	-	-	-	-
LV10	0-6 GPa	1028.8 (7)	3.9 (2)	-	-	-	-
LV11	0-10 GPa	1044.7 (9)	5.8 (2)	1045	4.6 (2)	-	-
OH1	0-6 GPa	3669.0 (8)	1.6 (2)	3672	2.3 (5)	3661	2.3 (1)
OH1	7-10 GPa	3636.5 (28)	6.3 (4)	-	-	-	-
OH2	0-6 GPa	3698.6 (4)	1.9 (1)	3698	2.3 (1)	3698	2.6 (1)
OH2	7-10 GPa	3684.1 (24)	4.0 (3)	-	-	-	-
OH3	7-10 GPa	3640.3 (48)	12.3 (6)	-	-	-	-

356 *LV 7 and 8 are clearly resolved bands in our spectra. However, when fitting them "together",
357 the resulting values are ν = 678.4 cm^{-1} and dν/d*P* = 5.7 cm^{-1}/GPa. 1-σ fitting uncertainties on the
358 last digit are given in brackets. [#]Large data scatter at pressures > 7 GPa for LV6.

359

360

References

Auzende, A.L., Daniel, I., Reynard, B., Lemaire, C., and Guyot, F. (2004) High-pressure behaviour of serpentine minerals: a Raman spectroscopic study. Physics and Chemistry of Minerals, 31, 269-277.

Balan, E., Saitta, A.M., Mauri, F., Lemaire, C., and Guyot, F. (2002) First-principles calculation of the infrared spectrum of lizardite. American Mineralogist, 87, 1286-1290.

Bezacier, L., Reynard, B., Bass, J.D., Sanchez-Valle, C., and Van de Moortèle, B. (2010) Elasticity of antigorite, seismic detection of serpentinites, and anisotropy in subduction zones. Earth and Planetary Science Letters, 289, 198-208.

Bezacier, L., Reynard, B., Cardon, H., Montagnac, G., and Bass, J.D. (2013) High-pressure elasticity of serpentine and seismic properties of the hydrated mantle wedge. Journal of Geophysical Research: Solid Earth, 118, 1-9.

Campione, M., and Capitani, G.C. (2013) Subduction-zone earthquake complexity related to frictional anisotropy in antigorite. Nature Geoscience, 6, 847-851.

Capitani, G.C., and Mellini, M. (2004) The modulated crystal structure of antigorite: The m = 17 polysome. American Mineralogist, 89, 147-158.

Capitani, G.C., and Mellini, M. (2006) The crystal structure of a second antigorite polysome (m = 16), by single-crystal synchrotron diffraction. American Mineralogist, 91, 394-399.

Capitani, G.C., and Stixrude, L. (2012) A first-principle investigation of antigorite up to 30 GPa: Structural behavior under compression. American Mineralogist, 97, 1177-1186.

Deschamps, F., Godard, M., Guillot, S., and Hattori, K. (2013) Geochemistry of subduction zone serpentinites: A review. Lithos, 178, 96-127.

Dobson, D.P., Meredith, P.G., and Boon, S.A. (2002) Simulation of Subduction Zone Seismicity by Dehydration of Serpentine. Science, 298, 1407-1410.

385 Gregorkiewitz, M., Lebech, B., Mellini, M., and Viti, C. (1996) Hydrogen positions and thermal
386 expansion in lizardite-1T from Elba; a low-temperature study using Rietveld refinement of
387 neutron diffraction data. American Mineralogist, 81, 1111-1116.
388 Hilairet, N., Reynard, B., Wang, Y., Daniel, I., Merkel, S., Nishiyama, N., and Petitgirard, S.
389 (2007) High-Pressure Creep of Serpentine, Interseismic Deformation, and Initiation of
390 Subduction. Science, 318, 1910-1913.
391 Kantor, I., Prakapenka, V., Kantor, A., Dera, P., Kurnosov, A., Sinogeikin, S., Dubrovinskaia, N.,
392 and Dubrovinsky, L. (2012) BX90: A new diamond anvil cell design for X-ray diffraction and
393 optical measurements. Review of Scientific Instruments, 83, 125102.
394 Katayama, I., Hirauchi, K.-i., Michibayashi, K., and Ando, J.-i. (2009) Trench-parallel
395 anisotropy produced by serpentine deformation in the hydrated mantle wedge. Nature, 461, 1114-
396 1117.
397 Koch-Müller, M., Speziale, S., Deon, F., Mrosko, M., and Schade, U. (2011) Stress-induced
398 proton disorder in hydrous ringwoodite. Physics and Chemistry of Minerals, 38, 65-73.
399 Libowitzky, E. (1999). Correlation of O-H Stretching Frequencies and O-H O Hydrogen Bond
400 Lengths in Minerals. In P. Schuster and W. Mikenda, Eds., Hydrogen Bond Research, 103-115,
401 Springer Vienna,
402 Long, M.D. (2013) Constraints on subduction geodynamics from seismic anisotropy. Reviews of
403 Geophysics, 51, 76-112.
404 Mao, H.-k., Xu, J., and Bell, P.M. (1986) Calibration of the ruby pressure gauge to 800 kbar
405 under quasi-hydrostatic conditions. Journal of Geophysical Research, 91, 4673-4676.
406 Marquardt, H., and Marquardt, K. (2012) Focused Ion Beam preparation and characterization of
407 single-crystal samples for high-pressure experiments in the diamond-anvil cell. American
408 Mineralogist, 97, 299-304.

Mellini, M., Trommsdorff, V., and Compagnoni, R. (1987) Antigorite polysomatism: behaviour during progressive metamorphism. Contributions to Mineralogy and Petrology, 97, 147-155.

Mookherjee, M., and Capitani, G.C. (2011) Trench parallel anisotropy and large delay times: Elasticity and anisotropy of antigorite at high pressures. Geophysical Research Letters, 38, L09315.

Mookherjee, M., and Stixrude, L. (2009) Structure and elasticity of serpentine at high-pressure. Earth and Planetary Science Letters, 279, 11-19.

Nestola, F., Angel, R., Zhao, J., Garrido, C., Sánchez-Vizcaíno, V., Capitani, G., and Mellini, M. (2010) Antigorite equation of state and anomalous softening at 6 GPa: an in situ single-crystal X-ray diffraction study. Contributions to Mineralogy and Petrology, 160, 33-43.

Noguchi, N., Moriwaki, T., Ikemoto, Y., and Shinoda, K. (2012) OH group behavior and pressure-induced amorphization of antigorite examined under high pressure and temperature using synchrotron infrared spectroscopy. American Mineralogist, 97, 134-142.

Reynard, B. (2013) Serpentine in active subduction zones. Lithos, 178, 171-185.

Reynard, B., and Wunder, B. (2006) High-pressure behavior of synthetic antigorite in the MgO-SiO_2-H_2O system from Raman spectroscopy. American Mineralogist, 91, 459-462.

Rinaudo, C., Gastaldi, D., and Belluso, E. (2003) Characterization of chrysotile, antigorite and lizardite by FT-Raman Spectroscopy. The Canadian Mineralogist, 41, 883-890.

Speziale, S., Marquardt, H., and Duffy, T.S. (2014). Brillouin Scattering in Geosciences. In G. S. Henderson, D. R. Neuville and R. T. Downs, Eds., Spectroscopic methods in mineralogy and materials science, 78, 543-603, Reviews in Mineralogy and Geochemistry, Mineralogical Society of America, Chantilly, Virginia.

Stixrude, L. (2002) Talc under tension and compression: Spinodal instability, elasticity, and structure. Journal of Geophysical Research: Solid Earth, 107, 2327.

433 Tsuchiya, J. (2013) A first-principles calculation of the elastic and vibrational anomalies of
434 lizardite under pressure. American Mineralogist, 98, 2046-2052.
435 Ulmer, P., and Trommsdorff, V. (1995) Serpentine Stability to Mantle Depths and Subduction-
436 Related Magmatism. Science, 268, 858-861.
437 Wunder, B., and Schreyer, W. (1997) Antigorite: High-pressure stability in the system MgO-
438 SiO_2-H_2O (MSH). Lithos, 41, 213-227.

439

440
441
442
443 **Figure 1** (color online): Antigorite single-crystal sample used in this study. (a) A sample for
444 DAC experiments was cut perpendicular to the basal plane by using the focused ion beam
445 technique (details in Marquardt and Marquardt, 2012). (b) An electron transparent foil was
446 prepared parallel to the DAC-sample from the same single-crystal (STEM bright field image). (c)
447 Electron diffraction pattern taken from the orange highlighted part of the TEM lamella (with the
448 [010] zone axis aligned to the incident beam).

449

450 **Figure 2**: Representative Raman spectra collected in the DAC at 0.7 GPa along with the best-fit
451 models. The most prominent lattice modes that were tracked to high pressures are labeled. (a)
452 Spectral region showing features related to lattice vibrational modes. (b) Spectral region related
453 to the OH stretching vibrations in antigorite.

454

455 **Figure 3** (color online): (a) Evolution of Raman spectra with pressure. Spectra were vertically
456 offset to enhance visibility. The change of the LV7 and LV8 is highlighted by green and blue
457 thick lines to illustrate the intensity crossover at around 6 GPa (left). The orange line illustrates
458 the appearance of the new band in the OH stretching region (right).

459 **Figure 4:** Raman shifts as a function of pressure for (a) lattice vibrational modes (strongest bands
460 are shown as full symbols), (b) LV3 and LV11, where the lines represent linear fits to the data
461 points below 6 GPa, and (c) OH stretching vibrational modes.
462
463 **Figure 5:** Dependence of Raman scattering amplitude on rotation angle for (a) the inner OH and
464 (b) the outer OH modes. At 0° and ambient pressure, the polarization of the incoming laser light
465 is about parallel to the **a** direction; at 90°, it is about parallel to **c**. Data collected at different
466 pressures were vertically offset to enhance visibility.
467
468 **Figure 6** (color online): (a) Brillouin spectrum of single-crystal antigorite at 5.3 GPa. (b)
469 Measured compressional velocity spatial distribution in a-c-plane of antigorite at 0.7 GPa (full
470 symbols) and 7.1 GPa (open symbols). The approximate locations of the **a**- and **c**-axes are
471 indicated. Error bars denote fitting uncertainties. Grey curves are fits to the experimental data
472 assuming orthorhombic symmetry of antigorite at 0.7 GPa (full curve) and 7.1 GPa (dotted
473 curve). The colored curves show results taken from previously published studies at our
474 experimental pressure: Blue: Mookherjee and Capitani (2011); green: Bezacier et al. (2013). (c)
475 Angle from **a** direction (rotation around **b**), where the minimum of compressional velocities
476 (black circles) were observed. Uncertainties in angles of minimum v_p are estimated from the
477 observed scattering of the experimental data. Literature data are shown for comparison.
478
479 **Figure 7:** (a) Compressional velocities of antigorite measured along **a** direction (circles) and **c**
480 direction (diamonds). An uncertainty in derived velocities of 0.1 km/s was assumed to account
481 for the small deviation of probed phonon propagation direction from the crystallographic axes.
482 Reported unit cell volumes from the computational study were converted to pressures by using

the computational equation of state parameters derived using the generalized gradient approximation (GGA) (Mookherjee and Capitani, 2011). (b) p-wave anisotropy in % (between v_p along **c** and **a** defined as $(v_{p,c}-v_{p,a})/(v_{p,c}+v_{p,a})*200$) of antigorite samples with different compositions. (c) Temperature dependence of acoustic velocities along **b**.

Figure 8: (a) p-wave anisotropy (defined as in Fig. 6) of antigorite as a function of iron-content and (b) aluminium-content. (c, d) shear wave polarization anisotropy along **b** at ambient pressure. Lines are linear fits.

Figure 1

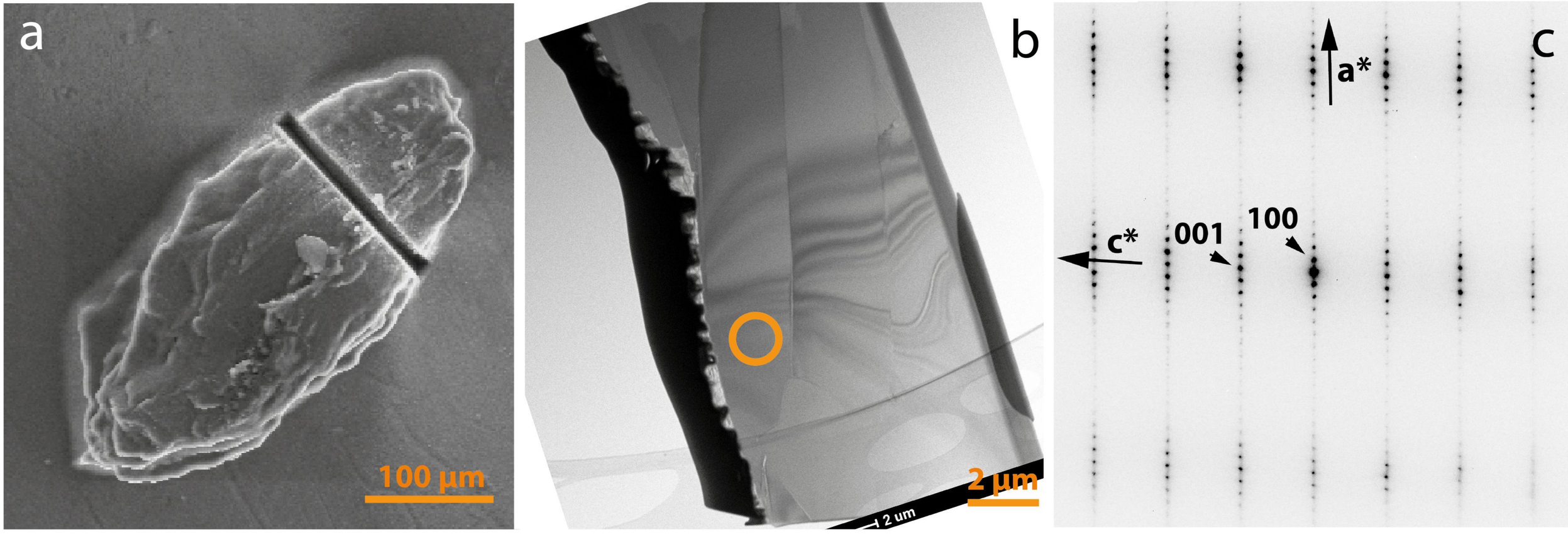

Figure 2

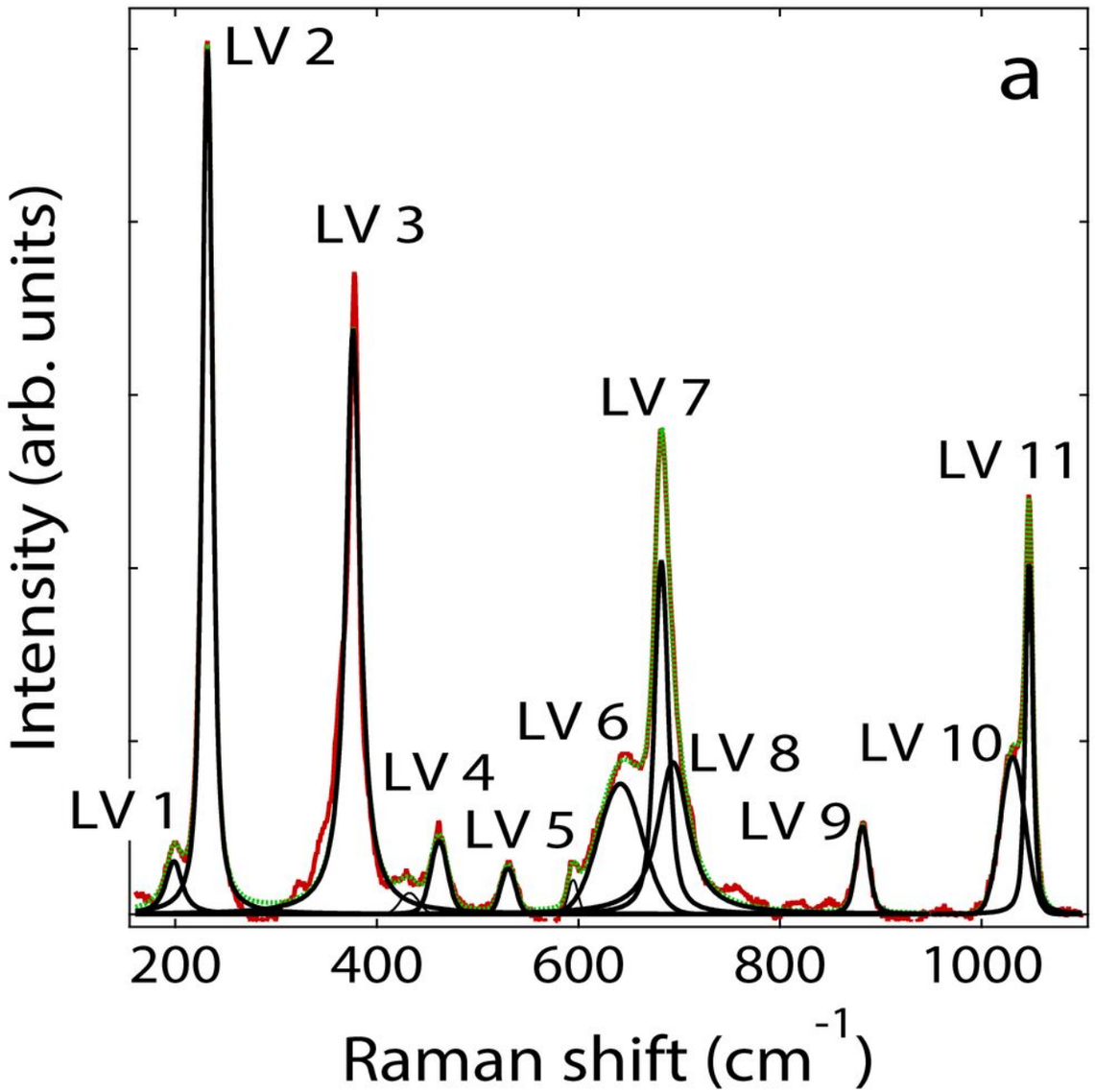
a
LV 1
LV 2
LV 3
LV 4
LV 5
LV 6
LV 7
LV 8
LV 9
LV 10
LV 11
Intensity (arb. units)
200
400
600
800
1000
Raman shift (cm-1)

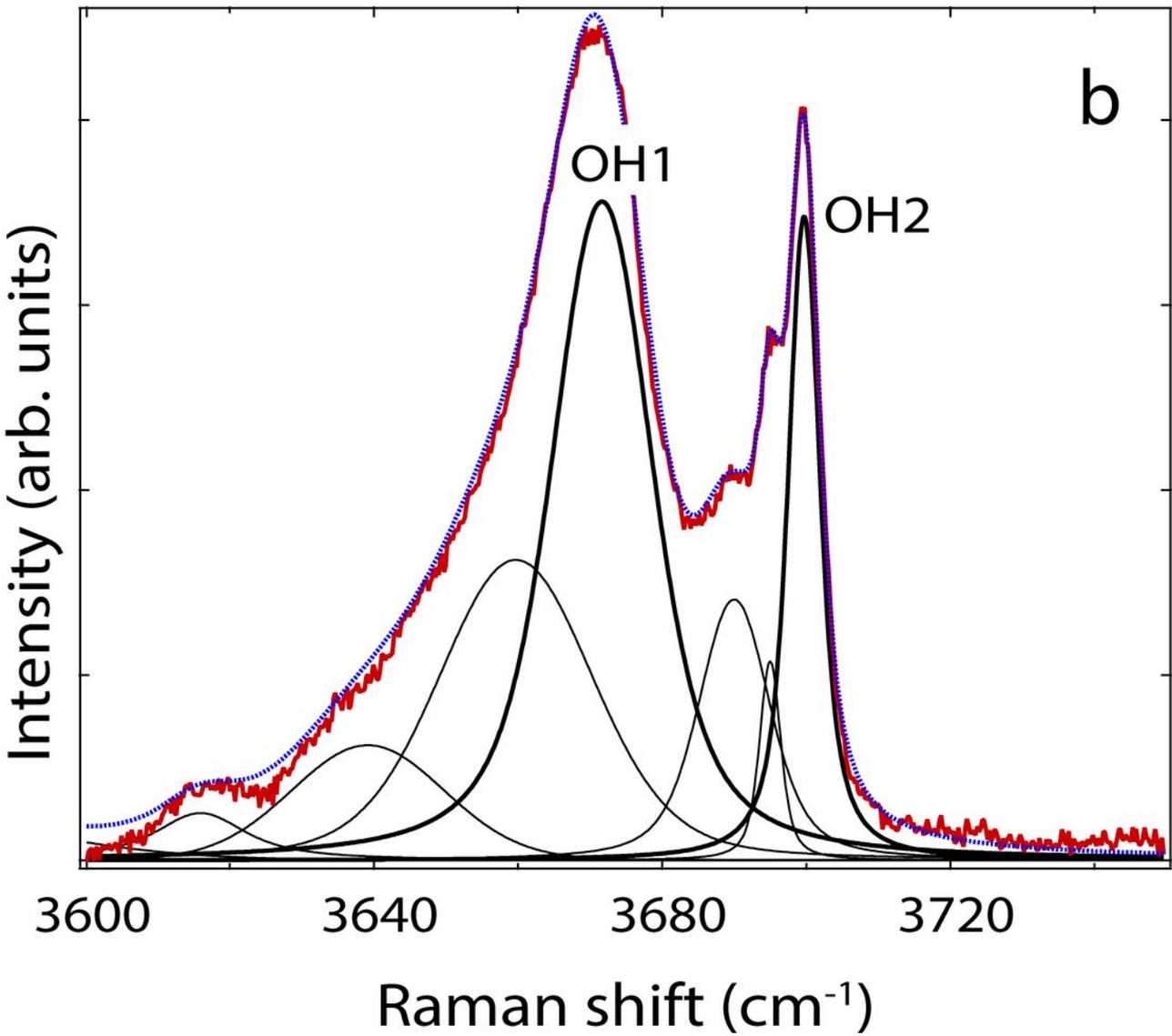
b
OH1
OH2
Intensity (arb. units)
3600
3640
3680
3720
Raman shift (cm-1)

Figure3

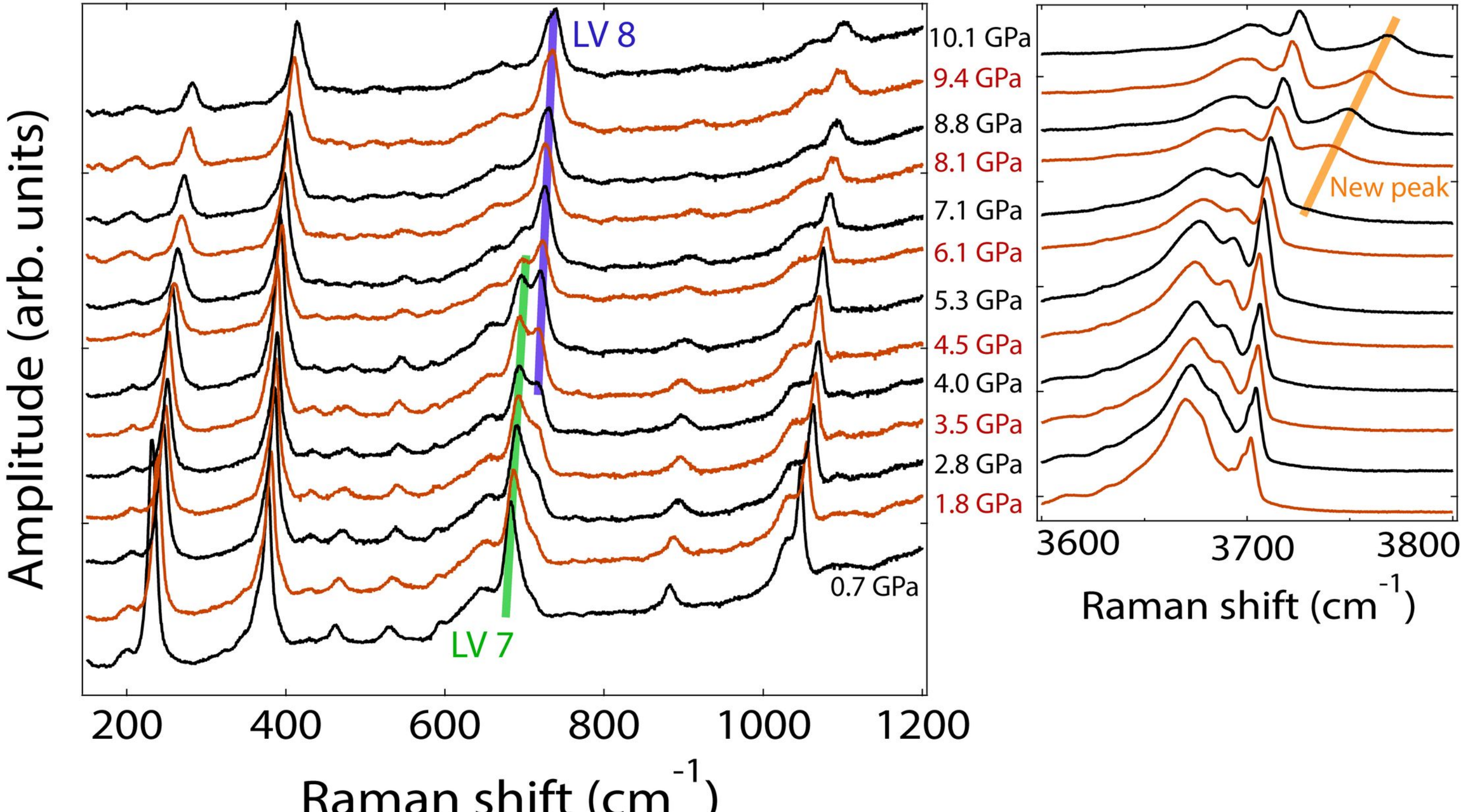
LV 8
LV 7
10.1 GPa
9.4 GPa
8.8 GPa
8.1 GPa
7.1 GPa
6.1 GPa
5.3 GPa
4.5 GPa
4.0 GPa
3.5 GPa
2.8 GPa
1.8 GPa
0.7 GPa
New peak
Amplitude (arb. units)
200
400
600
800
1000
1200
Raman shift (cm-1)
3600
3700
3800
Raman shift (cm-1)

Figure 4

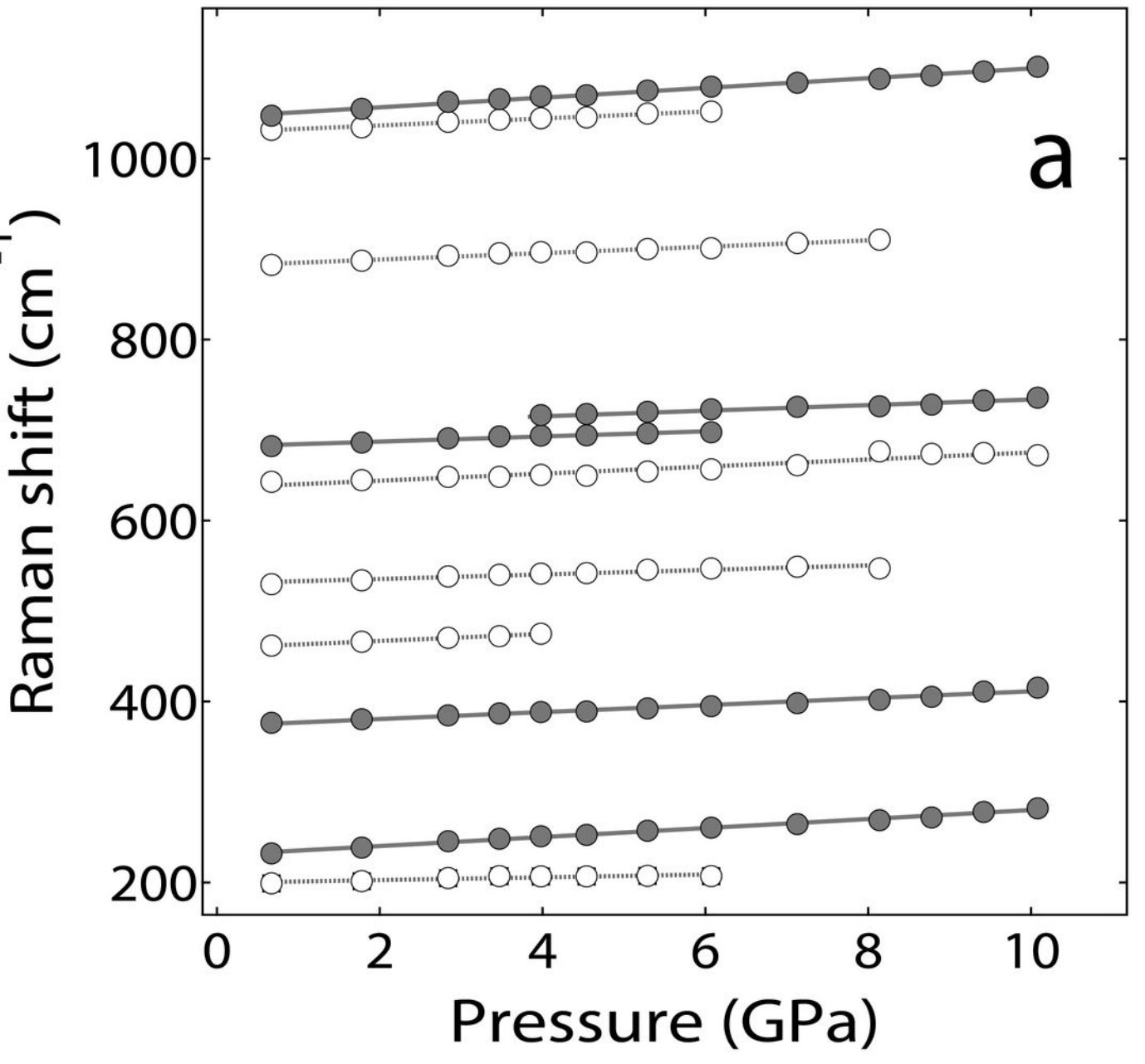
a
Raman shift (cm-1)
1000
800
600
400
200
0
2
4
6
8
10
Pressure (GPa)

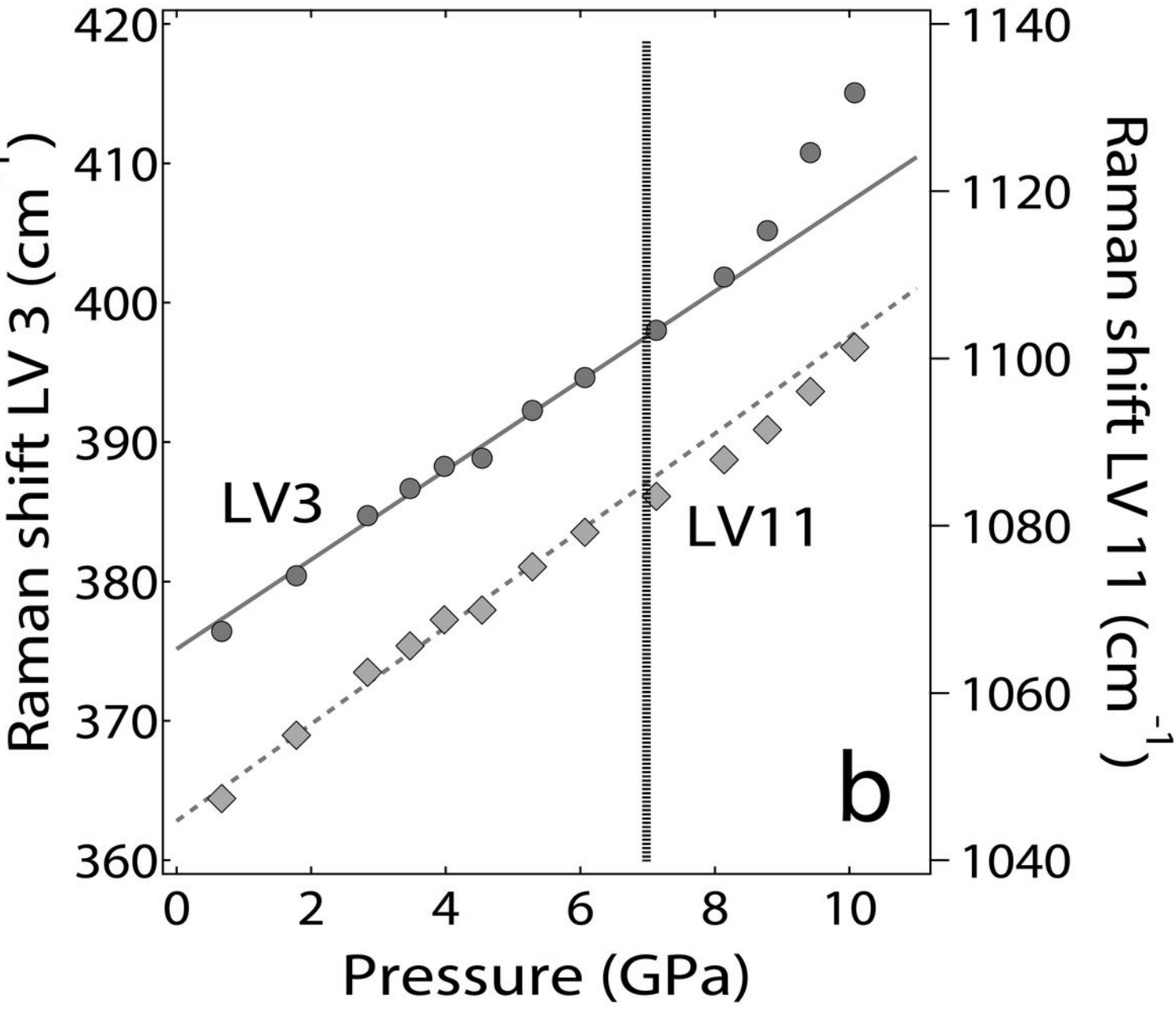
LV3
LV11
b
Raman shift LV 3 (cm-1)
Raman shift LV11 (cm-1)
420
410
400
390
380
370
360
1140
1120
1100
1080
1060
1040
0
2
4
6
8
10
Pressure (GPa)

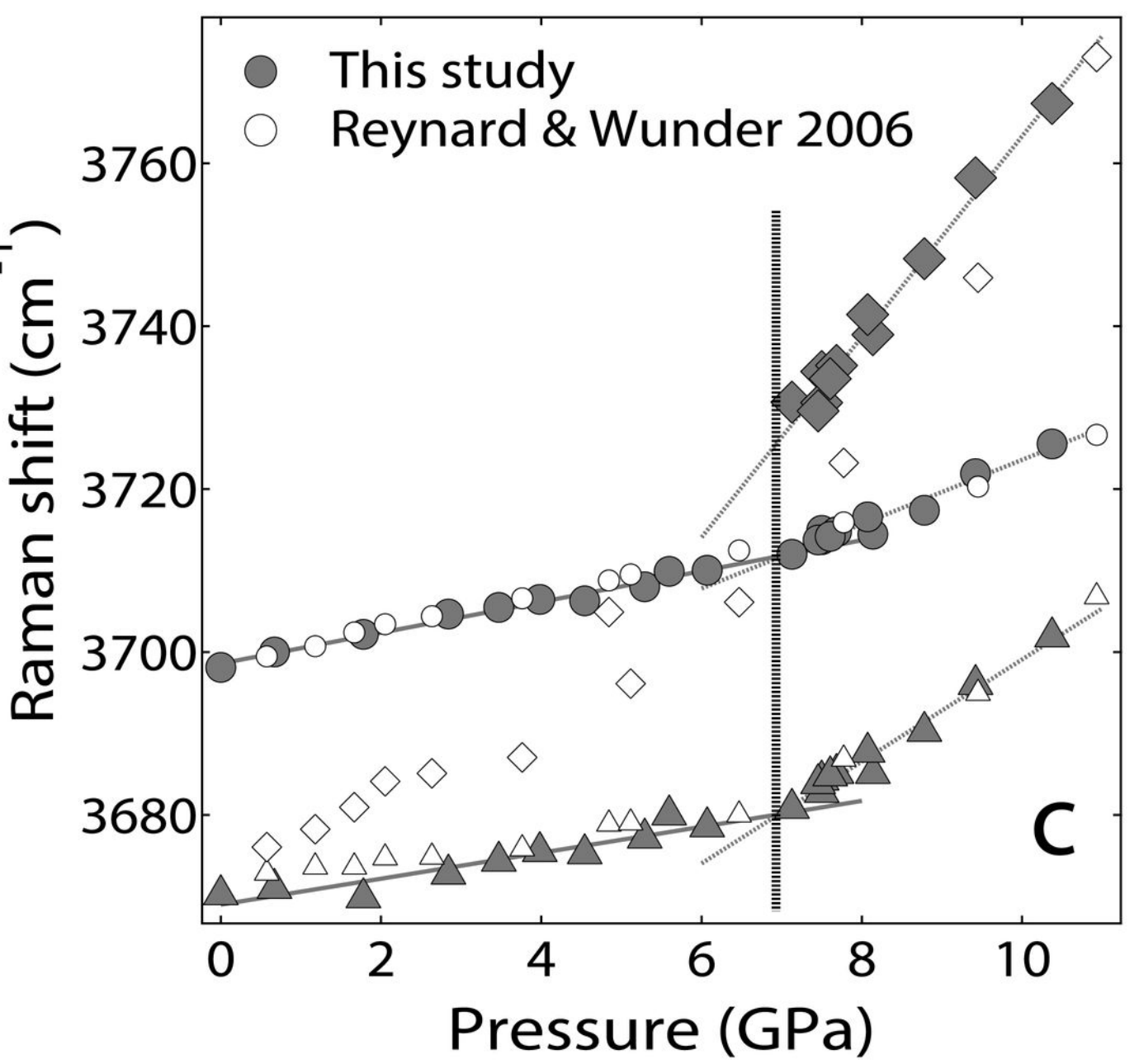
This study
Reynard & Wunder 2006
c
Raman shift (cm-1)
3760
3740
3720
3700
3680
0
2
4
6
8
10
Pressure (GPa)

Figure 5

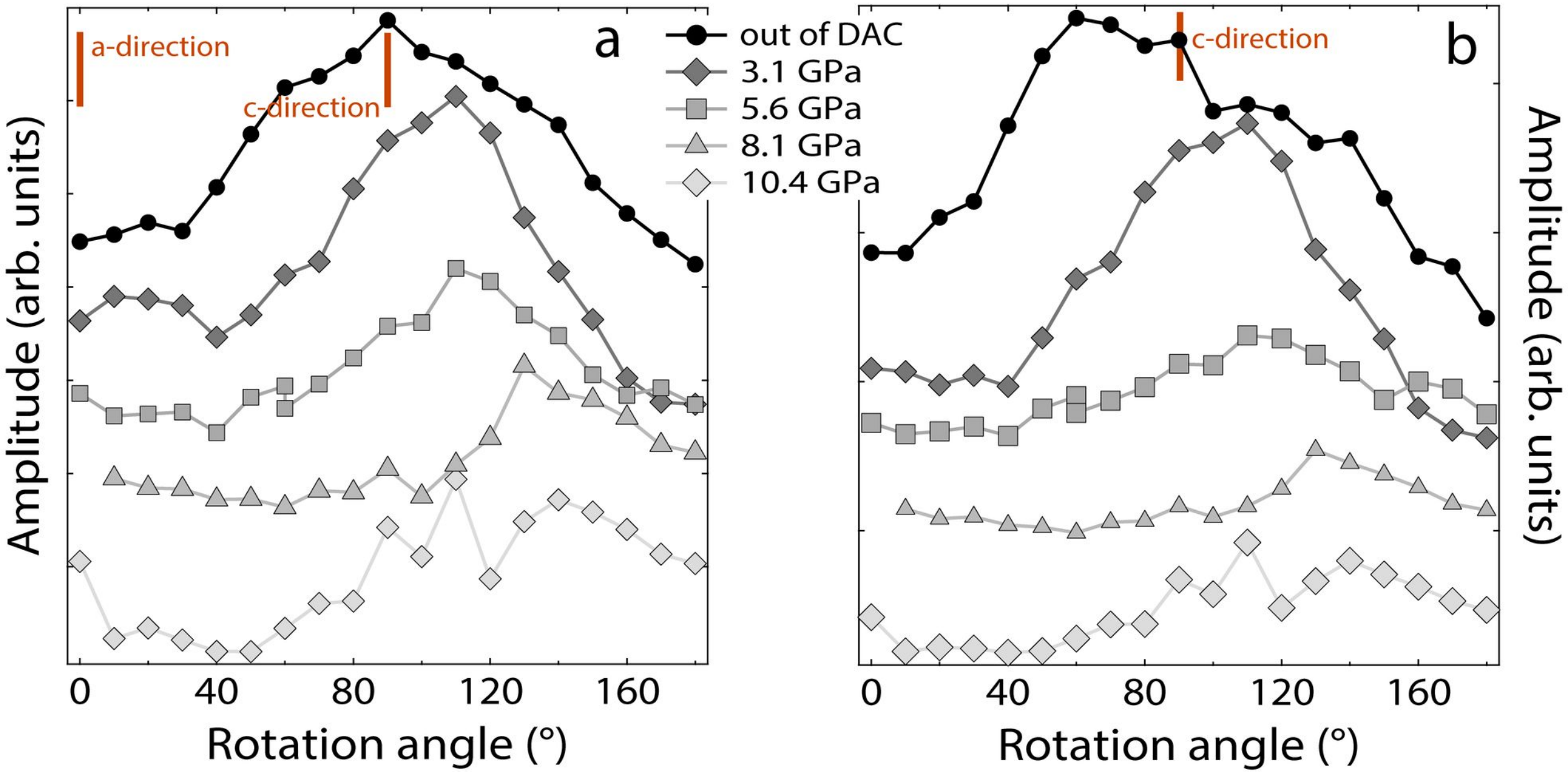
a
b
a-direction
c-direction
c-direction
out of DAC
3.1 GPa
5.6 GPa
8.1 GPa
10.4 GPa
Amplitude (arb. units)
Amplitude (arb. units)
0
40
80
120
160
0
40
80
120
160
Rotation angle (°)
Rotation angle (°)

Figure 6

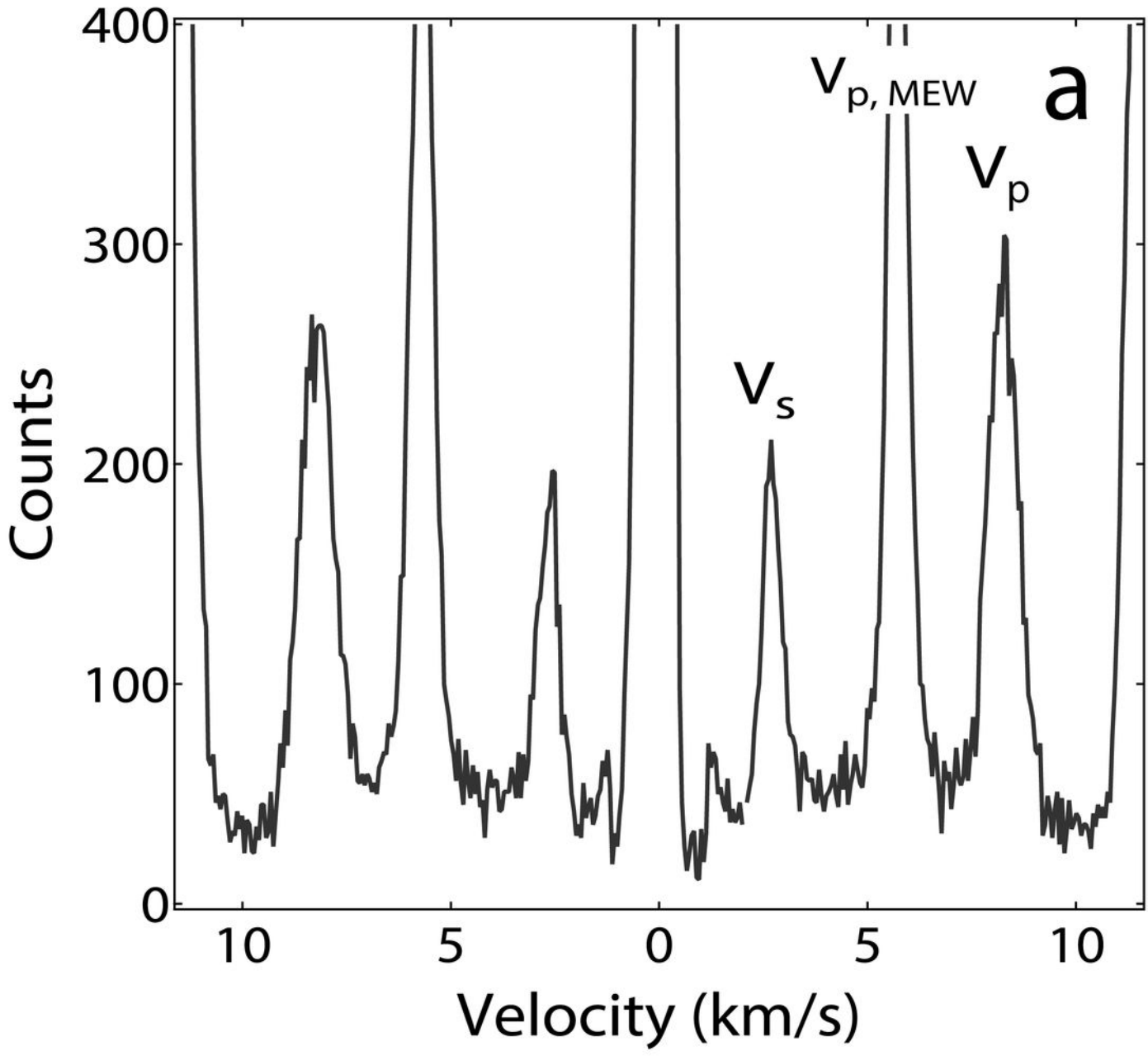
400
300
200
100
0
Counts
10
5
0
5
10
Velocity (km/s)
$v_{p, MEW}$
v_p
v_s
a

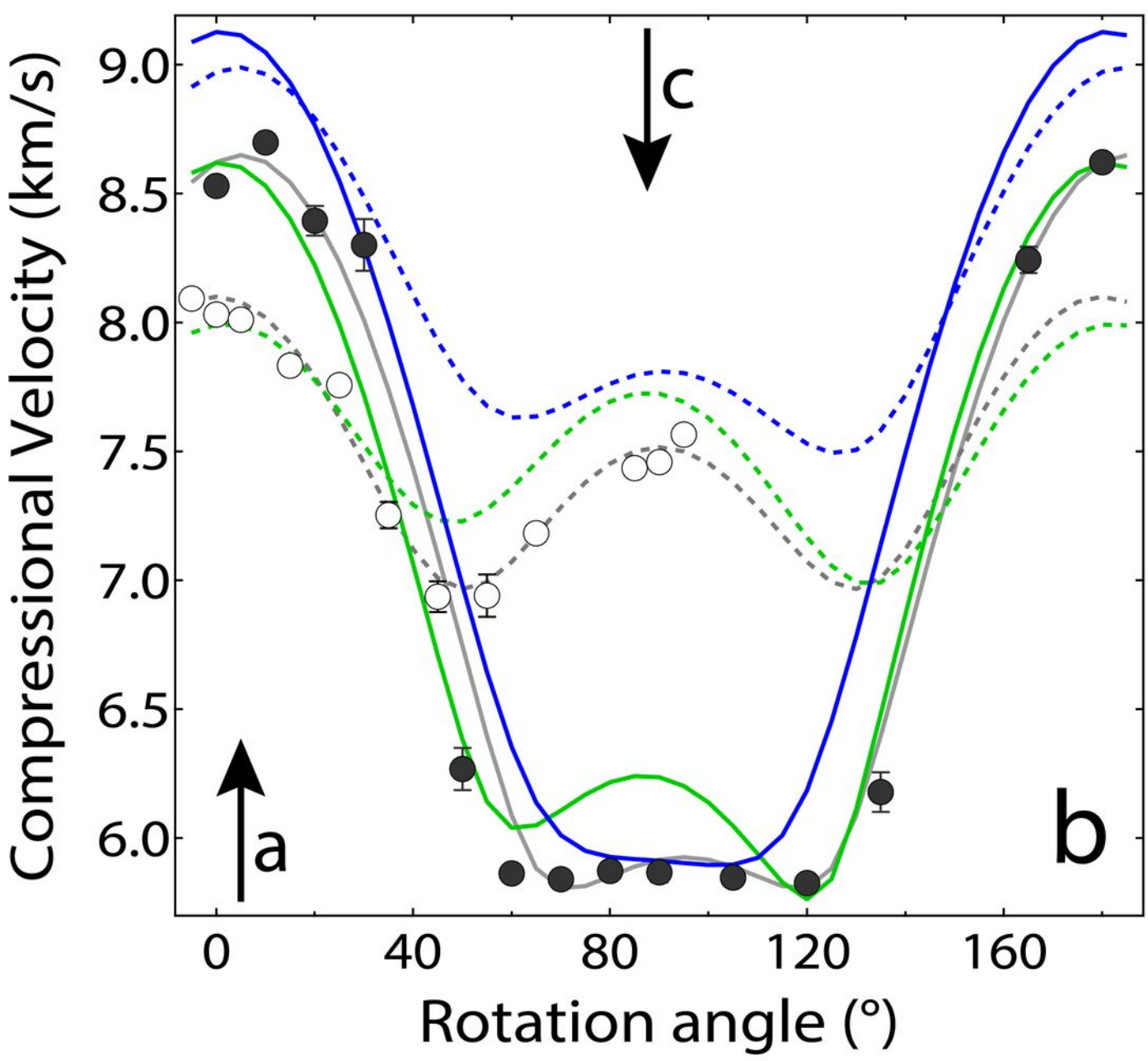
9.0
8.5
8.0
7.5
7.0
6.5
6.0
Compressional Velocity (km/s)
c
a
b
0
40
80
120
160
Rotation angle (°)

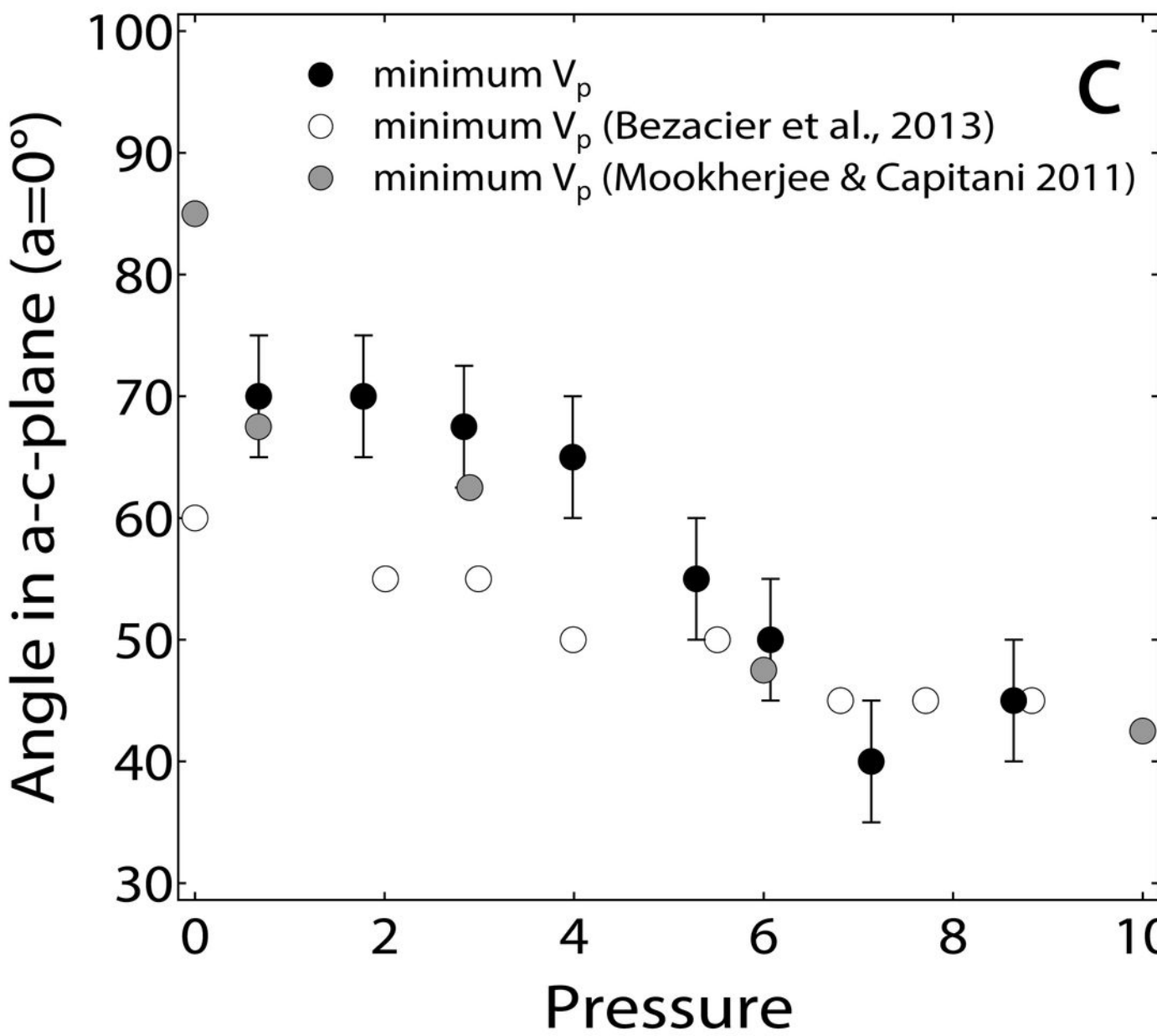
100
90
80
70
60
50
40
30
Angle in a-c-plane (a=0°)
minimum V_p
minimum V_p (Bezacier et al., 2013)
minimum V_p (Mookherjee & Capitani 2011)
c
0
2
4
6
8
10
Pressure

Figure 7

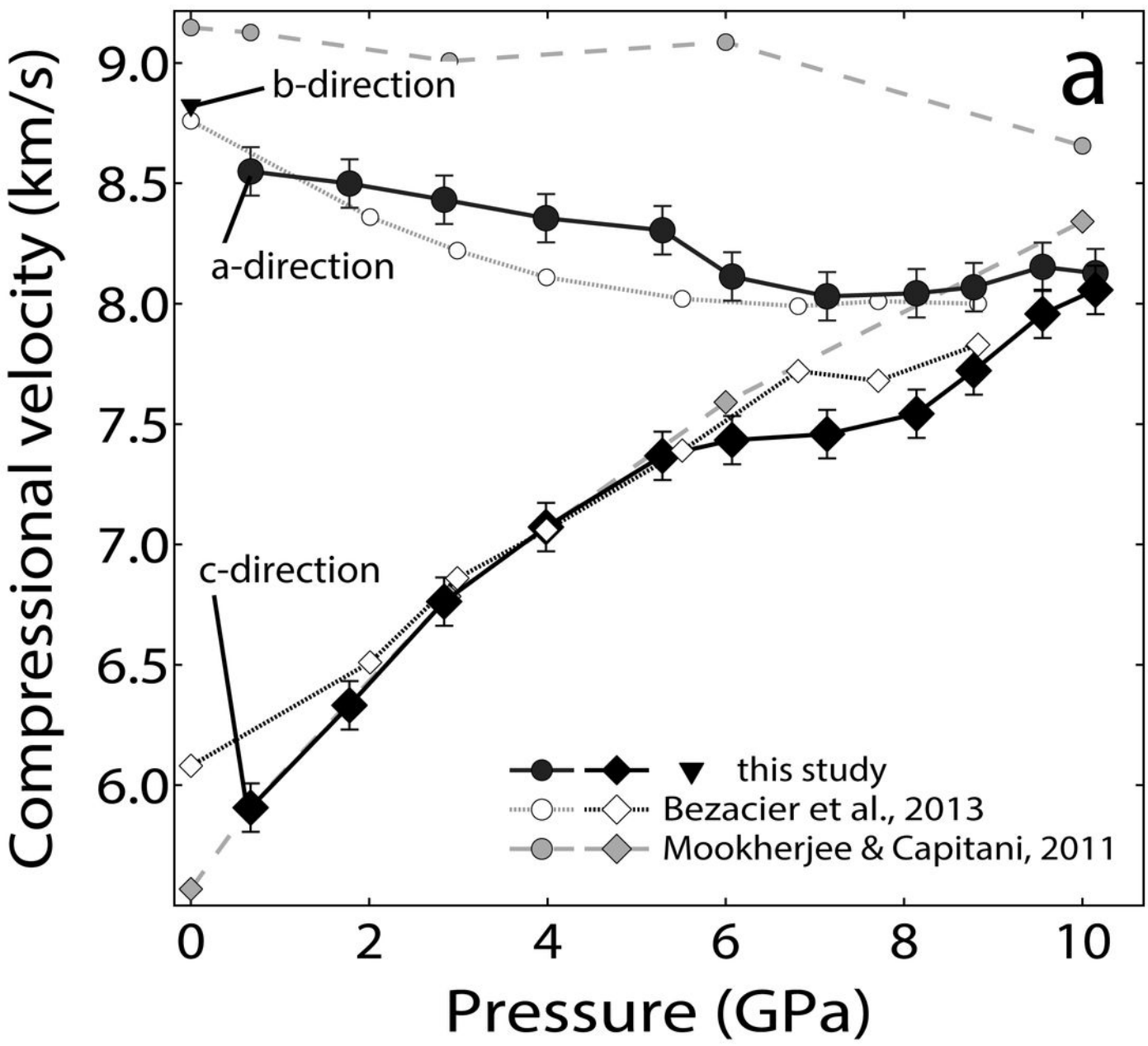
a
b-direction
a-direction
c-direction
this study
Bezacier et al., 2013
Mookherjee & Capitani, 2011
Compressional velocity (km/s)
Pressure (GPa)

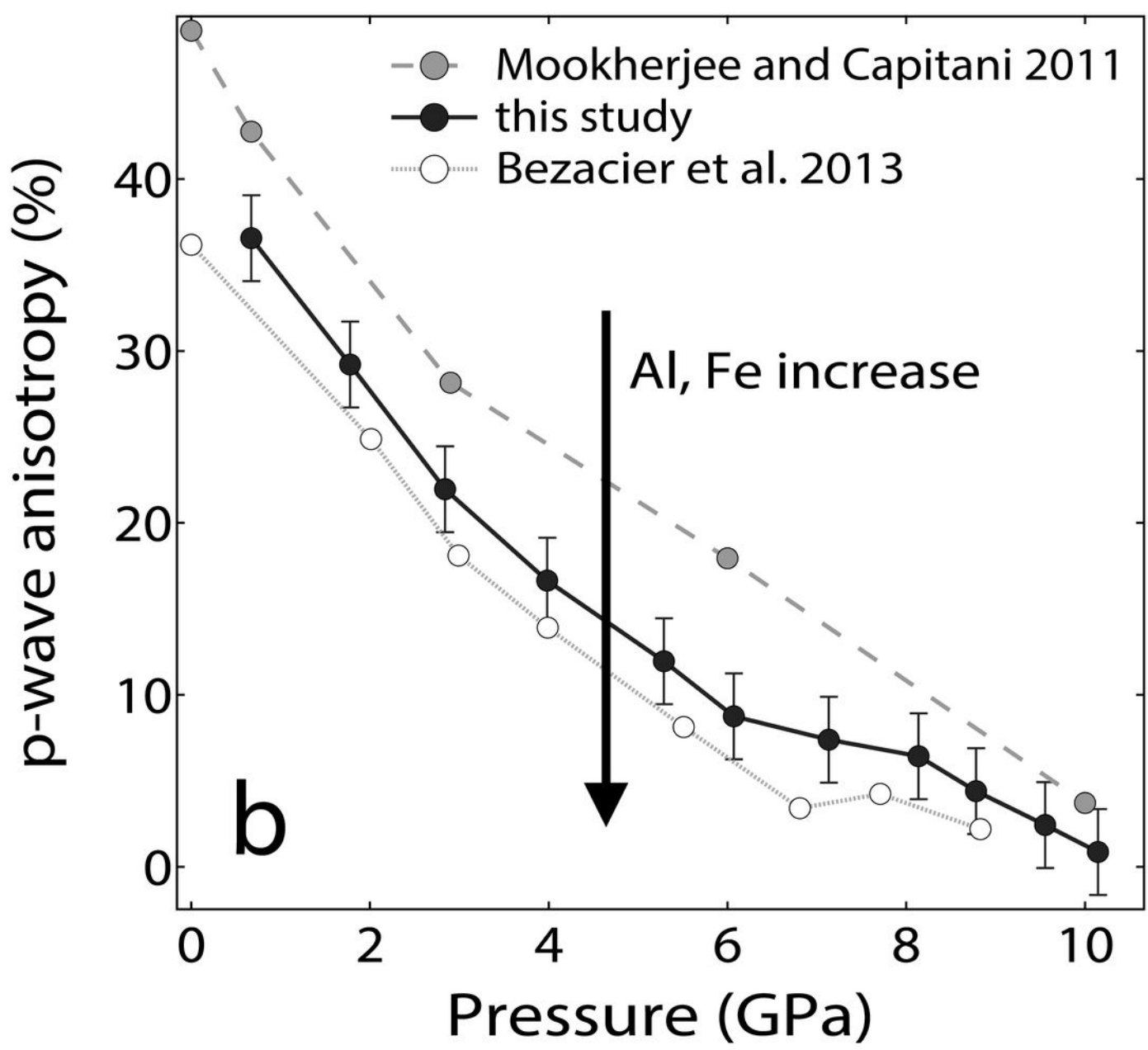
Mookherjee and Capitani 2011
this study
Bezacier et al. 2013
Al, Fe increase
b
p-wave anisotropy (%)
Pressure (GPa)

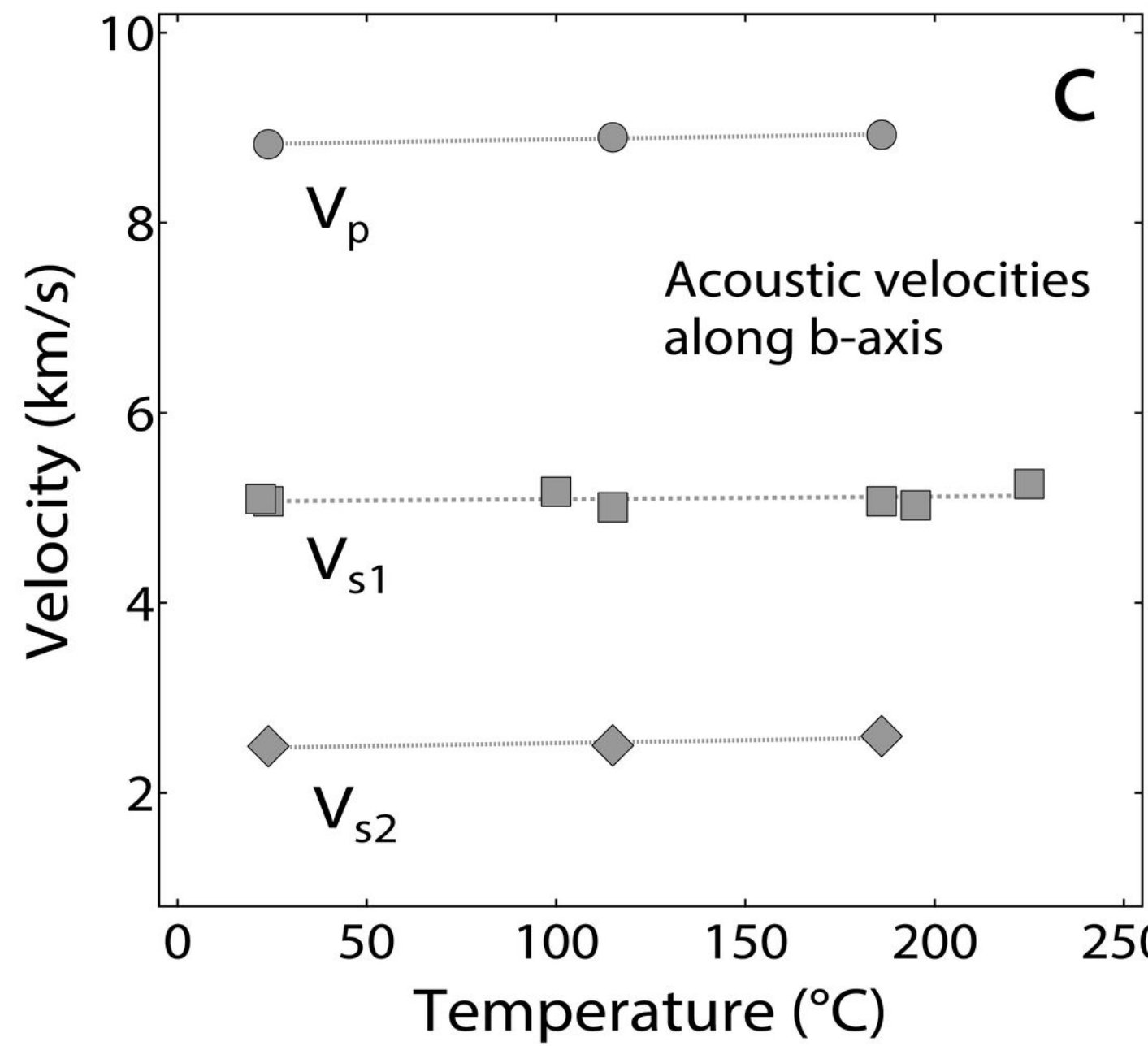
c
V_p
V_{s1}
V_{s2}
Acoustic velocities
along b-axis
Velocity (km/s)
Temperature (°C)

Figure 8

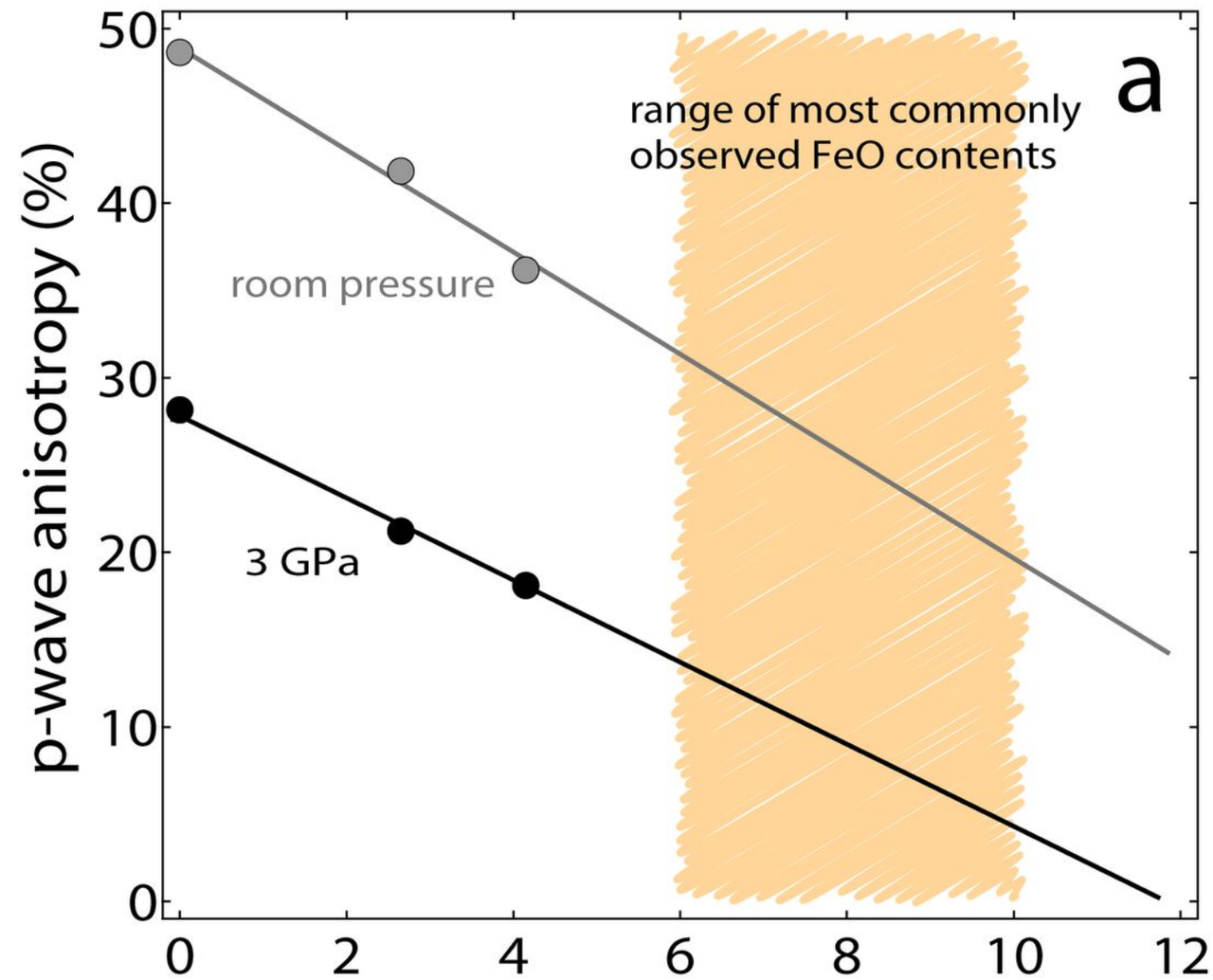

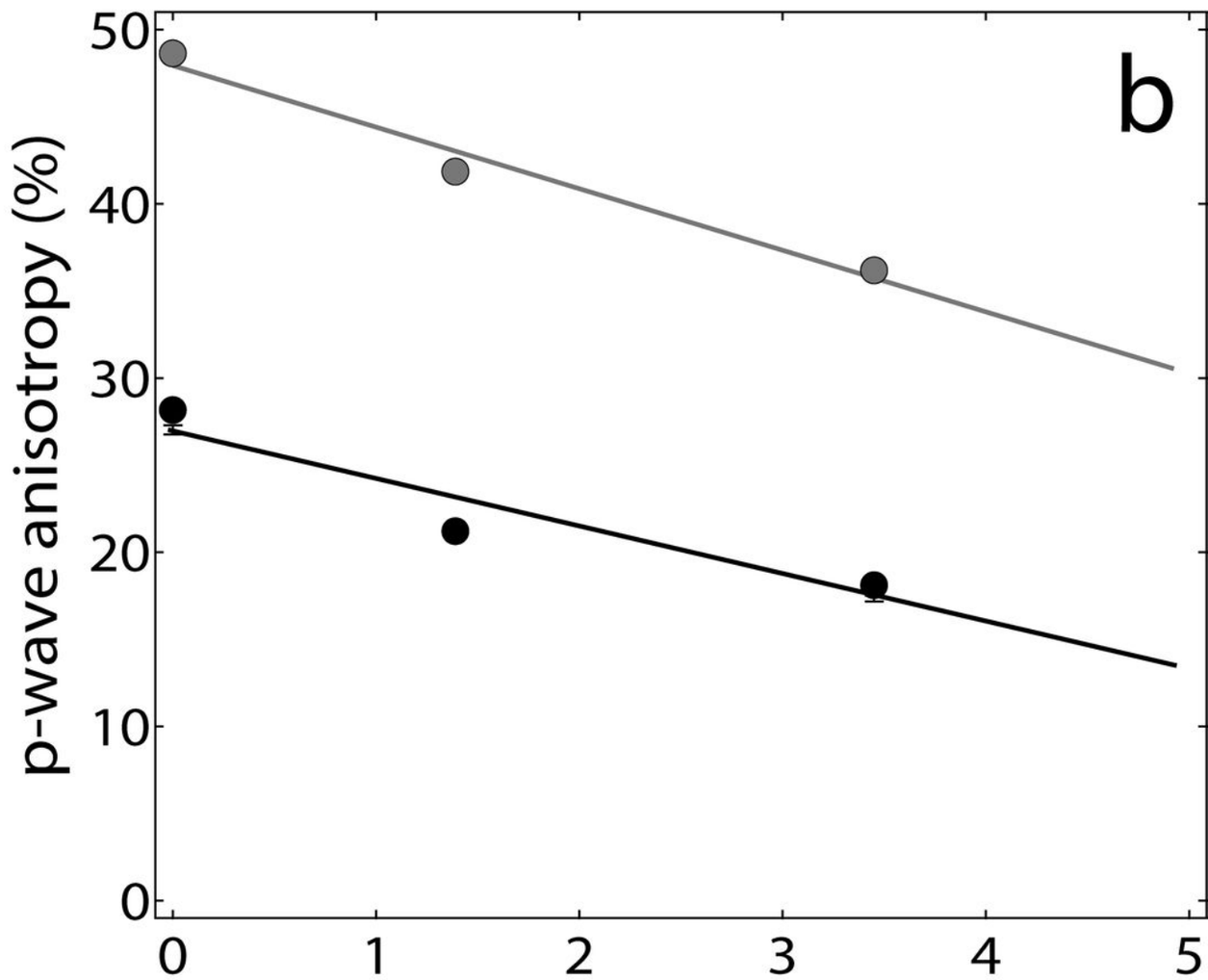

FeO (wt.%)

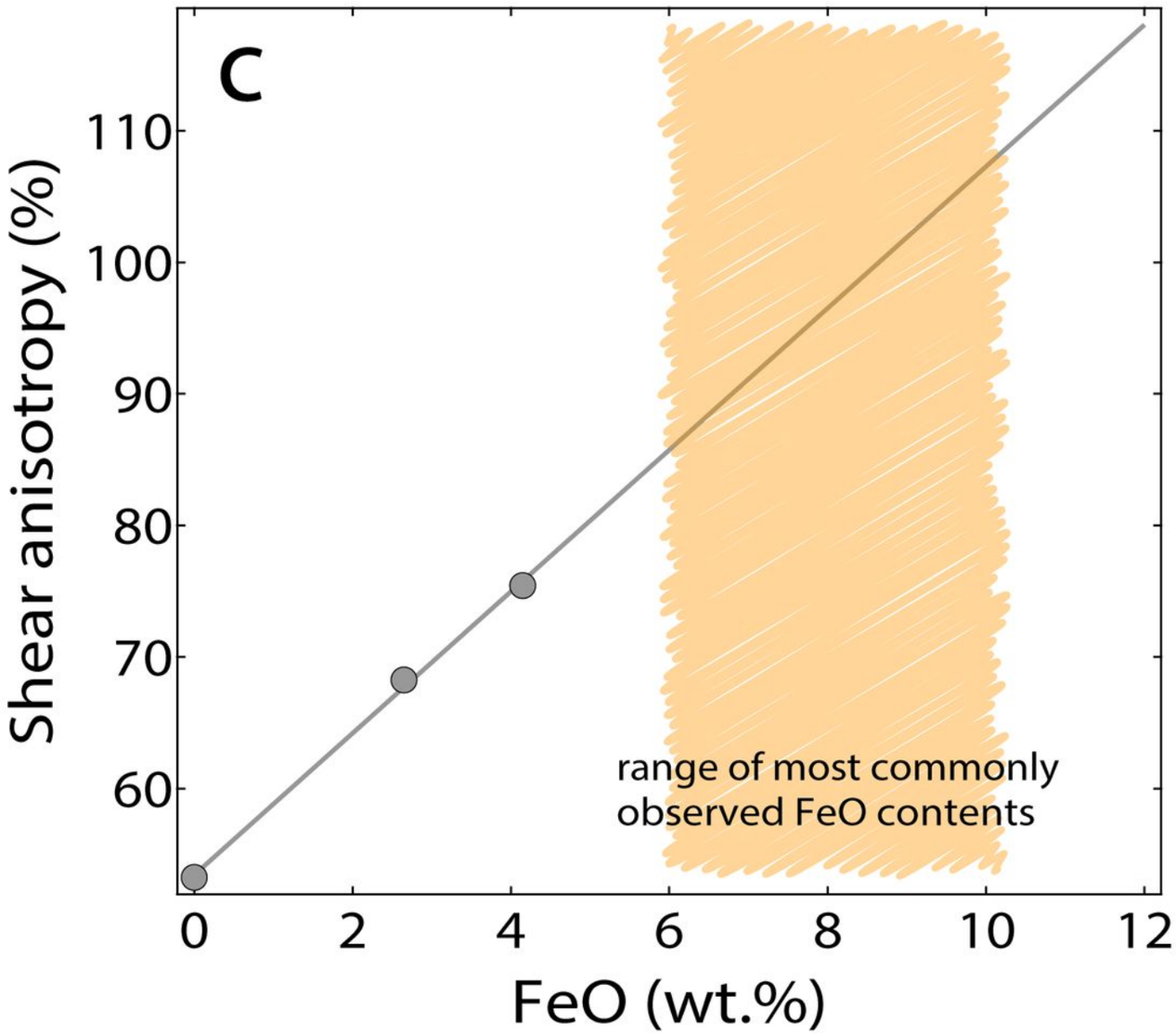

Al_2O_3 (wt.%)